grains (boxes in Fig. 4) in agreement with our atomistic simulations. During loading at ~40 GPa, our MD simulations predict a dislocation density of $\sim 10^{13}$ cm^{-2}, which is expected to decrease during recovery. Although the exact dislocation density in recovered samples is difficult to estimate, our high-resolution TEM images do show residual dislocations inside some nanograins (Fig. 4). This is quite unusual in nanocrystalline materials and not easily achievable under normal deformation conditions (*28*). Our experiments also indicate an increase in hardness in the samples recovered after shock loading, as expected from the measured residual dislocation densities.

Computer simulations of shocks in nanocrystalline copper show that the flow stress reaches ultrahigh values at high pressures produced by shock loading. This hardness increase of up to a factor of two compared with unshocked samples arises because the barriers for GB sliding increase with pressure (*13*–*15*), whereas dislocation nucleation is not as sensitive to pressure above a threshold of several gigapascals. Although the simulations we have carried out are for nanocrystalline copper, GB sliding reduction under pressure should be a general feature of shock-loaded materials, including alloy and nonmetallic nanocrystals. Harder nanocrystalline materials could offer novel applications, including improved armor materials and National Ignition Facility targets (*5*).

References and Notes

1. R. Madec, B. Devincre, L. Kubin, T. Hoc, D. Rodney, *Science* **301**, 1879 (2003).
2. M. A. Meyers, K. K. Chawla, *Mechanical Behavior of Materials* (Prentice-Hall, Upper Saddle River, NJ, 1999).
3. J. R. Weertman, in *Nanostructured Materials: Processing, Properties and Potential Applications*, C. C. Koch, Ed. (William Andrew, Norwich, NY, 2002), pp. 397–421.
4. J. Schiøtz, K. W. Jacobsen, *Science* **301**, 1357 (2003).
5. T. R. Dittrich *et al.*, *Laser Part. Beams* **17**, 217 (1999).
6. D. Jia, K. T. Ramesh, E. Ma, L. Lu, K. Lu, *Scripta Mater.* **45**, 613 (2001).
7. L. Lu, S. X. Li, K. Lu, *Scripta Mater.* **45**, 1163 (2001).
8. F. Dalla Torre *et al.*, *Acta Mater.* **50**, 3957 (2002).
9. B. L. Holian, P. S. Lomdahl, *Science* **280**, 2085 (1998).
10. B. A. Remington *et al.*, *Metall. Mater. Trans. A* **35**, 2587 (2004).
11. M. A. Meyers *et al.*, *Acta Mater.* **51**, 1211 (2003).
12. J. M. McNaney, J. Edwards, R. Becker, T. Lorenz, B. A. Remington, *Metall. Trans. A* **35**, 2625 (2004).
13. C. A. Schuh, A. C. Lund, *Nat. Mater.* **2**, 449 (2003).
14. A. C. Lund, C. A. Schuh, *Acta Mater.* **53**, 3193 (2005).
15. B. Jiang, G. J. Weng, *J. Mech. Phys. Solids* **52**, 1125 (2004).
16. Materials and methods are available as supporting material on *Science* Online.
17. H. Van Swygenhoven, A. Caro, *Phys. Rev. B* **58**, 11246 (1998).
18. H. Van Swygenhoven, M. Spaczer, A. Caro, D. Farkas, *Phys. Rev. B* **60**, 22 (1999).
19. J. Schiøtz, F. D. Di Tolla, K. W. Jacobsen, *Nature* **391**, 561 (1998).
20. V. Yamakov *et al.*, *Nat. Mater.* **1**, 45 (2002).
21. H. Van Swygenhoven, P. M. Derlet, A. G. Frøseth, *Nat. Mater.* **3**, 399 (2004).
22. M. W. Chen, J. W. McCauley, K. J. Hemker, *Science* **299**, 1563 (2003).
23. K. Kadau, T. C. Germann, P. S. Lomdahl, B. L. Holian, *Science* **296**, 1681 (2002).
24. E. Bringa *et al.*, *J. App. Phys.* **96**, 3793 (2004).
25. F. A. Sapozhnikov, V. V. Dremov, M. S. Smirnova, *J. Phys. IV France* **110**, 323 (2003).
26. L. Davila *et al.*, *Appl. Phys. Lett.* **86**, 161902 (2005).
27. S. Cheng, J. A. Spencer, W. W. Milligan, *Act. Mater.* **51**, 4505 (2003).
28. Z. Budrovic, H. Van Swygenhoven, P. M. Derlet, S. Van Petegem, B. Schmitt, *Science* **304**, 273 (2004).

29. We thank A. M. Hodge and C. A. Schuh for help with the experiments; P. Erhart for calculating elastic constants; D. Farkas, T. Diaz de la Rubia, R. Lebensohn, M. A. Meyers, V. Bulatov, N. Park, and V. Dremov for useful discussions; M. Duchaineau for plotting the results; and Livermore Computing for MCR and Thunder time. This work was performed under the auspices of the U.S. Department of Energy at Lawrence Livermore National Laboratory under contract no. W-7405-Eng-48, with support from the Laboratory Directed Research and Development program.

Supporting Online Material

www.sciencemag.org/cgi/content/full/309/5742/1838/DC1
Materials and Methods
Figs. S1 to S4
Movies S1 and S2
References

29 June 2005; accepted 18 August 2005
10.1126/science.1116723

Influence of the Atlantic Subpolar Gyre on the Thermohaline Circulation

Hjálmar Hátún,[1,2]* Anne Britt Sandø,[3,4] Helge Drange,[3,4,5,6] Bogi Hansen,[1] Heðinn Valdimarsson[7]

During the past decade, record-high salinities have been observed in the Atlantic Inflow to the Nordic Seas and the Arctic Ocean, which feeds the North Atlantic thermohaline circulation (THC). This may counteract the observed long-term increase in freshwater supply to the area and tend to stabilize the North Atlantic THC. Here we show that the salinity of the Atlantic Inflow is tightly linked to the dynamics of the North Atlantic subpolar gyre circulation. Therefore, when assessing the future of the North Atlantic THC, it is essential that the dynamics of the subpolar gyre and its influence on the salinity are taken into account.

Formation of the densest, deepest waters of the North Atlantic THC occurs following the northward flow of warm, saline waters (the Atlantic Inflow) (Fig. 1) across the Greenland-Scotland Ridge. Through air-sea exchange, these waters subsequently lose much of their heat, but not their salt. Added freshwater from precipitation and river runoff reduces the salinity somewhat but still allows them to become the densest waters in the region. This makes the Arctic Mediterranean—the Arctic Ocean and the Nordic Seas—the dominant source area for the North Atlantic THC (*1*, *2*). Because the density close to the freezing point is mainly determined by the salinity, changes in the upper-layer salinities of this region may have large impacts on the future development of this circulation.

Climate models featuring increasing greenhouse-gas scenarios predict an intensified freshwater supply to the Arctic Mediterranean during the 21st century (*3*). Observations indicate that this is already occurring (*4*, *5*) and that large areas are freshening (*5*–*7*). This freshwater increase may partly explain why many climate models indicate a weakening of the North Atlantic THC starting from the end

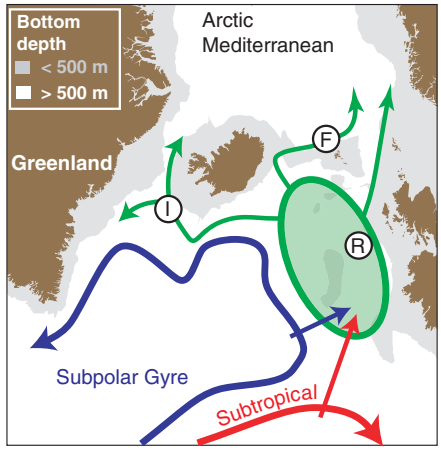

Fig. 1. Schematic of the main features of the surface circulation in the northeastern North Atlantic. The green shaded region shows where the subpolar and the subtropical waters meet, mix, and feed into the Arctic Mediterranean. The hydrographic observations used in the study are obtained in the Rockall Trough (R), Faroe Current (F), and Irminger Current (I).

[1]Faroese Fisheries Laboratory, Box 3051, FO-110, Tórshavn, Faroe Islands. [2]University of Washington, Box 357940, Seattle, WA 98195, USA. [3]Nansen Environmental and Remote Sensing Center, Thormøhlensgt. 47, N-5006 Bergen, Norway. [4]Bjerknes Center for Climate Research, Allégaten 55, 5007 Bergen, Norway. [5]Geophysical Institute University of Bergen, Allégaten 70, 5007 Bergen, Norway. [6]Nansen-Zhu International Research Centre, Institute of Atmospheric Physics, Chinese Academy of Sciences, Beijing 100029, China. [7]Marine Research Institute, Skúlagata 4, 121 Reykjavík, Iceland.

*To whom correspondence should be addressed. E-mail: hjalmarh@ocean.washington.edu

of the 20th century (*3*). Other models (*8*) predict a stable North Atlantic THC due to increasing salinities of the waters flowing toward the ventilation areas. This underscores the potential importance of recent observations that all three branches of the Atlantic Inflow to the Arctic Mediterranean (*9*) have shown increasing salinities during the last decade, with record-high values in 2003 (Fig. 2). This salinity anomaly has already been seen to influence the Arctic Mediterranean, and at Ocean Weather Station Mike in the Norwegian Sea (66°N, 2°E), the poleward-flowing Atlantic Water reached salinity values (and temperatures) in 2004 that were higher than ever since the observations started in 1948 (*10*, *11*). These changes may be expected to have large impacts on the high-latitude climate system and its populations and ecosystems, although the detailed responses are difficult to predict.

The climate system is, however, strongly influenced by internal variability modes, which have to be distinguished from the fingerprints of the more gradual global warming. The Atlantic Inflow into the Arctic Mediterranean is drawn from both the North Atlantic subpolar gyre (SPG) and subtropical gyre (STG) (Fig. 1). Four possible mechanisms may explain the observed record-high salinity of the Atlantic Inflow: (i) changes in the (local) air-sea flux of freshwater [evaporation minus precipitation (E – P)]; (ii) increasing salinities of the STG water; (iii) increasing salinities of the SPG water; and (iv) dynamic changes in the relative contributions from the two gyres. Here, we discuss these four alternatives by combining observations and results from a numerical Ocean General Circulation Model (OGCM). This is the Nansen Center version (*12*–*14*) of the MICOM (Miami Isopycnal Coordinate Ocean Model) (*15*), forced with daily mean National Centers for Environmental Prediction/National Center for Atmospheric Research (NCEP/NCAR) (*16*) reanalyses of fresh water, heat, and momentum fluxes for the period 1948 to 2003. Simulated fields from this model system compare favorably with observations in the northeastern Atlantic and Nordic Seas (*13*, *17*, *18*) and simulate the salinity variations of the three Atlantic Inflow branches accurately (fig. S1).

To test the explanatory power of mechanism (i), the (E – P) field, obtained from the NCEP/NCAR reanalyses, has been integrated over a box centered on the eastern SPG region, giving an index of the atmospheric freshwater flux (fig. S2). Comparing the temporal variation of this index to the observed upper-layer (*14*) salinity variations in the northeastern Atlantic, it is clear that the air-sea flux [mechanism (i)] cannot explain the observed record-high Atlantic Inflow salinities. This finding is consistent with other studies (*19*, *20*).

As for mechanism (ii), the STG salinity has been observed to increase (*5*, *21*). However, the salinity variations in the Atlantic Inflow (Figs. 1 and 2) do not correspond to the salinity variations in the STG (*22*) (fig. S3). Furthermore, the simulated salinity in the upper layers of the central SPG, mechanism (iii), shows no relation to the Atlantic Inflow salinity (fig. S3). For interannual to interdecadal time scales, neither mechanism (ii) nor (iii) seems able to explain the Atlantic Inflow salinity variations, which leaves only dynamical variations [e.g., mechanism (iv)] as a possible explanation.

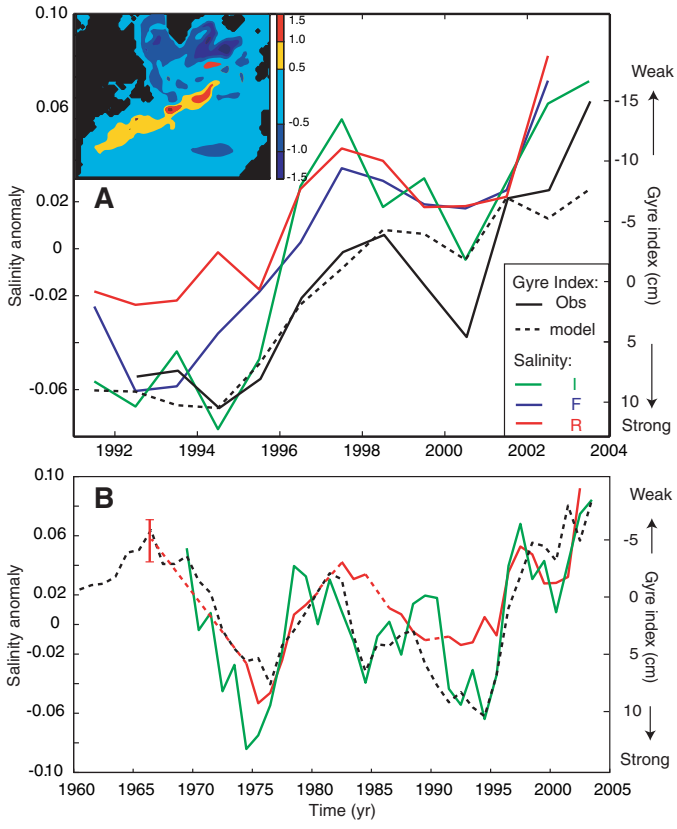

Fig. 2. Temporal evolution of key parameters. (**A**) Colored lines show annual averages of the observed salinity anomalies (*14*) in inflow areas R, F, and I in Fig. 1. The time series R and F are shifted 1 year backward, and the time series I is shifted 2 years backward to account for advective delays. The solid black line shows the principal component, the gyre index (inverted), associated with the leading North Atlantic sea-surface height mode, as obtained from altimetry observations. The dashed line represents the gyre index (inverted) obtained from MICOM. The inset shows the principal spatial mode of variability (EOF) of simulated sea-surface height (see also fig. S4B). (**B**) As in (A), but for a longer time period. The red vertical line in (B) indicates the approximate salinity range in the mid-1960s as deduced from surface salinity data (*26*).

Häkkinen and Rhines (*23*) described dynamical variations in the SPG during the decade 1992 to 2002 using altimeter data. A decline of the gyre circulation, as represented by the principal component (the "gyre index") from an empirical orthogonal function (EOF) analysis, is seen to parallel the increasing salinities in the northeastern Atlantic (Fig. 2A).

The altimetry observations used by Häkkinen and Rhines extend back only to 1992, but the analysis can be extended backward, using results from MICOM. During the 1992 to 2003 period, MICOM reproduces the Häkkinen and Rhines mode (the "gyre mode") both in terms of its spatial form (Fig. 2A, inset, and fig. S4) and its temporal variation (the gyre index) through the principal component (Fig. 2A). It is therefore reasonable to apply MICOM to put the changes into a longer time perspective and to explore causal relations. To do this, Fig. 2B compares the simulated gyre index with the salinities of the two Atlantic Inflow branches (I and R) for which long-term observations are available. It is seen that the correspondence between the Atlantic Inflow salinity and the gyre index is not limited to the period after 1992 but extends back at least to the mid 1960s.

The variability of the Atlantic Inflow salinities is part of a larger picture, which may be illustrated by the changes from a high-index year (1993) to a low-index year (1998) (Fig. 3). The main features are a southward shift of the frontal zone between the two gyres in the Newfoundland Basin and a substantial salinity increase along the eastern margin of the North Atlantic, including the Iceland Basin. Density changes in the northeastern Atlantic are governed mainly by changes in temperature, which have been very similar to the salinity changes (fig. S4, C and D). Replacement of the cold and dense water in the Iceland and Irminger Basins with warmer and lighter waters implies an increase in the sea-surface height, whereas colder water replacing warmer water in the Newfoundland Basin likewise implies a decrease in the sea-surface height. This is the pattern detected by the gyre mode, explaining a >15-cm increase in the Iceland and Irminger Basins and a decrease of similar magnitude in the Newfoundland Basin (inset in Fig. 2A). The gyre index is therefore related not only to the strength of the gyre circulation but also to the

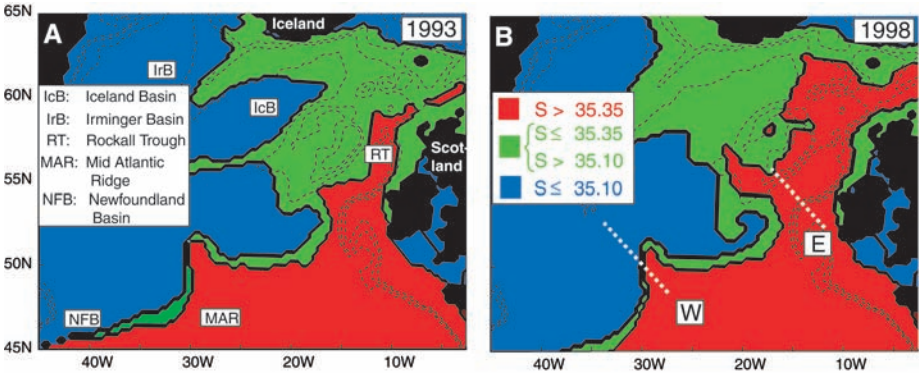

Fig. 3. The simulated upper-layer (*14*) spatial distribution of typical SPG water (blue), STG water (red), and a mixture, influenced by both gyres (green), averaged for the low-salinity year 1993 (**A**) and the high-salinity year 1998 (**B**). The 500-m, 1000-m, and 2000-m depth contours are outlined with dashed black lines, and two sections, one crossing the North Atlantic Current (W) and one covering the entrance to the Rockall Trough (E), are shown with dashed white lines.

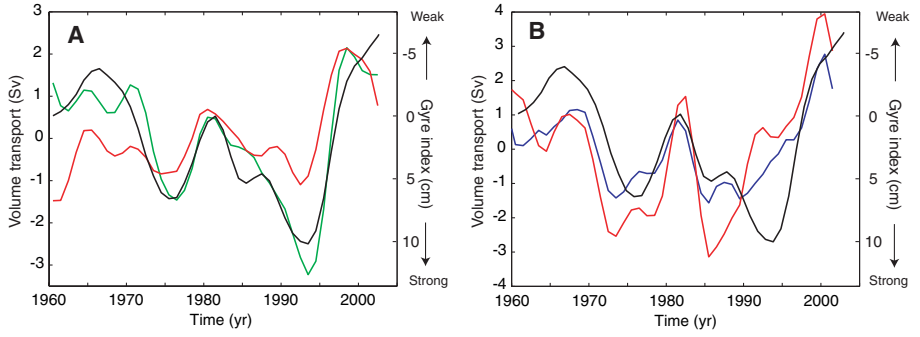

Fig. 4. Simulated anomalies of upper-layer (*14*) volume transport of different water masses through the two sections shown in Fig. 3B compared with the simulated gyre index (black; note inverse scales). (**A**) The transport anomaly of water with salinity below (green) and above (red) the 35.35 isohaline along section E (Fig. 3) into the Rockall Trough. (**B**) The transport anomaly of water with salinity below (blue) and above (red) 34.95 through section W (Fig. 3), crossing the North Atlantic Current (NAC). Annual averages, smoothed with a 3-year running mean, are shown. Positive values of transport anomalies for the red lines on (A) and (B) indicate anomalous transport toward the northeast. For the green line on (A) and the blue line on (B), positive values indicate anomalous transport toward the southwest.

shape of the gyre. During the high-index period in the early 1990s, the gyre had an east-west shape with strong protrusions into the eastern basins (Fig. 3A), whereas in the low-index years in the late 1990s, it had a more north-south shape, largely confined to the west of the Mid-Atlantic Ridge (Fig. 3B).

A more detailed understanding may be obtained by focusing on the Rockall Trough, which is a main passageway for the Atlantic Inflow. The upper layers of the trough are fed from two sources (*24*, *25*): water from the North Atlantic Current (NAC), which follows the boundary between the two gyres (green areas in Fig. 3), and water of more southern origin from areas west of and over the continental slope (eastern part of the red areas in Fig. 3). On a section across the trough (section E in Fig. 3B), the waters from the two sources are generally found to be separated by a front, which straddles the 35.35 isohaline (fig. S5). By extracting the volume transports on both sides of this front from MICOM, we obtain estimates of the influence of each of the two sources on the inflow through the trough. The result (Fig. 4A) clearly shows that the effect of the gyre circulation is to modulate the influence of the relatively fresh NAC on the inflow through the trough.

This influence may be traced upstream to section W across the NAC over the Mid Atlantic Ridge (Fig. 3B). In the model, this section consistently includes the entire frontal zone associated with the current, and the 34.95 isohaline encompasses the sectional area from which the transport of SPG water has been extracted (fig. S6). The transport of STG water through section W has been extracted from the region south of the front defined by the 34.95 isohaline. The resulting time series (Fig. 4B) do not follow the gyre index quite as well as for Fig. 4A, but they still strongly support that the SPG circulation is linked to the relative contributions from the two gyres to the NAC at this location: When the gyre index is high, the volume transport of SPG water through the section is also high and the volume transport of STG water is low, and vice versa for a low gyre index.

We conclude that on interannual to interdecadal time scales, the salinity of the Atlantic Inflow to the Arctic Mediterranean is controlled mainly by the dynamics of the SPG circulation and its effects on the location, intensity, and composition of the NAC in the northeastern Atlantic. This conclusion does not exclude the possibility that intensified evaporation in the tropical Atlantic and export of freshwater to the Pacific may affect the Atlantic Inflow salinity on longer time scales. According to some climate models (*3*, *8*), this may have a stabilizing effect on the THC. Our results demonstrate, however, that the recently observed record-high Atlantic Inflow salinities are not primarily a consequence of this mechanism and that the coupling between the tropical Atlantic and the Atlantic Inflow to the Arctic Mediterranean is highly dependent on the dynamics of the SPG. In periods with intensive SPG circulation, the stabilizing effect of increasing tropical salinities on the thermohaline ventilation in the Arctic Mediterranean will be reduced. The mechanisms that induce SPG variations were discussed by Häkkinen and Rhines (*23*), and these mechanisms and their response to human-induced global warming clearly merit more detailed investigations. That has not been the focus of this paper, but our results demonstrate that realistic description of these mechanisms in climate models is a precondition for reliable assessment of the future North Atlantic THC. Our results also show the key importance of long and continued observational time series for this purpose.

References and Notes

1. R. R. Dickson, J. Brown, *J. Geophys. Res.* **99**, 12319 (1994).
2. B. Hansen, S. Østerhus, D. Quadfasel, W. R. Turrell, *Science* **305**, 953 (2004).
3. U. Cubasch, G. Meehl, in *Climate Change 2001: The Scientific Basis*, J. T. Houghton *et al.*, Eds. (Cambridge Univ. Press, Cambridge, 2001), pp. 525–582.
4. B. J. Peterson *et al.*, *Science* **298**, 2171 (2002).
5. R. Curry, B. Dickson, I. Yashayaev, *Nature* **426**, 826 (2003).
6. J. Blindheim *et al.*, *Deep-Sea Res.* **47**, 655 (2000).
7. R. Curry, C. Mauritzen, *Science* **308**, 1772 (2005).
8. M. Latif, E. Roeckner, U. Mikolajewicz, R. Voss, *J. Clim.* **13**, 1809 (2000).
9. B. Hansen, S. Østerhus, *Prog. Oceanogr.* **45**, 109 (2000).
10. S. Østerhus, personal communication.
11. H. Drange *et al.*, in *The Nordic Seas: An Integrated Perspective, AGU Monograph 158*, H. Drange, T. Dokken, T. Furevik, R. Gerdes, W. Berger, Eds. (American Geophysical Union, Washington, DC, 2005), pp. 1–10.
12. M. Bentsen, H. Drange, T. Furevik, T. Zhou, *Clim. Dyn.* **22**, 701 (2004).
13. H. Drange *et al.*, in *The Nordic Seas: An Integrated Perspective, AGU Monograph 158*, H. Drange, T. Dokken, T. Furevik, R. Gerdes, W. Berger, Eds. (American Geophysical Union, Washington, DC, 2005), pp. 199–220.
14. Materials and methods are available as supporting material on *Science* Online.
15. R. Bleck, C. Rooth, C. Hu, L. T. Smith, *J. Phys. Oceanogr.* **22**, 1486 (1992).

16. E. Kalnay *et al.*, *Bull. Am. Meteorol. Soc.* **77**, 437 (1996).
17. J. E. Nilsen, Y. Gao, H. Drange, T. Furevik, M. Bentsen, *Geophys. Res. Lett.* **30**, 10.1029/2002GL016597 (2003).
18. H. Hátún, A. Sandø, H. Drange, M. Bentsen, in *The Nordic Seas: An Integrated Perspective, AGU Monograph 158*, H. Drange, T. Dokken, T. Furevik, R. Gerdes, W. Berger, Eds. (American Geophysical Union, Washington, DC, 2005), pp. 239–250.
19. M. Bersch, *J. Geophys. Res.* **107**, 10.1029/2001JC000901 (2002).
20. N. P. Holliday, *J. Geophys. Res.* **108**, 10.1029/2002JC001344 (2003).
21. T. P. Boyer, S. Levitus, J. I. Antonov, R. A. Locarnini, H. E. Garcia, *Geophys. Res. Lett.* **32**, 10.1029/2004GL021791 (2005).
22. T. M. Joyce, P. Robbins, *J. Clim.* **9**, 3121 (1996).
23. S. Häkkinen, P. B. Rhines, *Science* **304**, 555 (2004).
24. N. P. Holliday, R. T. Pollard, J. F. Read, H. Leach, *Deep-Sea Res.* **47**, 1303 (2000).
25. D. J. Ellett, J. H. A. Martin, *Deep-Sea Res.* **20**, 585 (1973).
26. D. J. Ellett, S. R. Jones, "Surface temperature and salinity time-series from the Rockall Channel, 1948-1992" (Fisheries research data report number 36, Ministry of Agriculture, Fisheries, and Food, Directorate of Fisheries Research, Lowestoft, 1994; www.cefas.co.uk/publications/files/datarep36.pdf).
27. We thank M. Bentsen for model development, P. Rhines for commenting on the paper; M. Miles for language editing, and S. Häkkinen for the extended gyre index in Fig. 2A, based on altimetry. The work is supported by the Nordic Council of Ministers program Vestnordisk Oceanklima; the Ocean Surface Topography Science Team of NASA; the Research Council of Norway through RegClim, NOClim, and the Program of Supercomputing; and the European Union DG-XII Climate and Environment Program through DYNAMITE (GOCE-0093903) and NOCES (EVK2-2001-00115).

Supporting Online Material
www.sciencemag.org/cgi/content/full/309/5742/1841/DC1
Materials and Methods
Figs. S1 to S6

12 May 2005; accepted 4 August 2005
10.1126/science.1114777

Changes in Tropical Cyclone Number, Duration, and Intensity in a Warming Environment

P. J. Webster,[1] G. J. Holland,[2] J. A. Curry,[1] H.-R. Chang[1]

We examined the number of tropical cyclones and cyclone days as well as tropical cyclone intensity over the past 35 years, in an environment of increasing sea surface temperature. A large increase was seen in the number and proportion of hurricanes reaching categories 4 and 5. The largest increase occurred in the North Pacific, Indian, and Southwest Pacific Oceans, and the smallest percentage increase occurred in the North Atlantic Ocean. These increases have taken place while the number of cyclones and cyclone days has decreased in all basins except the North Atlantic during the past decade.

During the hurricane season of 2004, there were 14 named storms in the North Atlantic, of which 9 achieved hurricane intensity. Four of these hurricanes struck the southeast United States in rapid succession, causing considerable damage and disruption. Analysis of hurricane characteristics in the North Atlantic (*1*, *2*) has shown an increase in hurricane frequency and intensity since 1995. Recently, a causal relationship between increasing hurricane frequency and intensity and increasing sea surface temperature (SST) has been posited (*3*), assuming an acceleration of the hydrological cycle arising from the nonlinear relation between saturation vapor pressure and temperature (*4*). The issue of attribution of increased hurricane frequency to increasing SST has resulted in a vigorous debate in the press and in academic circles (*5*).

Numerous studies have addressed the issue of changes in the global frequency and intensity of hurricanes in the warming world. Our basic conceptual understanding of hurricanes suggests that there could be a relationship between hurricane activity and SST. It is well established that SST > 26°C is a requirement for tropical cyclone formation in the current climate (*6*, *7*). There is also a hypothesized relationship between SST and the maximum potential hurricane intensity (*8*, *9*). However, strong interannual variability in hurricane statistics (*10*–*14*) and the possible influence of interannual variability associated with El Niño and the North Atlantic Oscillation (*11*, *12*) make it difficult to discern any trend relative to background SST increases with statistical veracity (*8*). Factors other than SST have been cited for their role in regulating hurricane characteristics, including vertical shear and mid-tropospheric moisture (*15*). Global modeling results for doubled CO_2 scenarios are contradictory (*15*–*20*), with simulations showing a lack of consistency in projecting an increase or decrease in the total number of hurricanes, although most simulations project an increase in hurricane intensity.

Tropical ocean SSTs increased by approximately 0.5°C between 1970 and 2004 (*21*). Figure 1 shows the SST trends for the tropical cyclone season in each ocean basin. If the Kendall trend analysis is used, trends in each of the ocean basins are significantly different from zero at the 95% confidence level or higher, except for the southwest Pacific Ocean. Here we examine the variations in hurricane characteristics for each ocean basin in the context of the basin SST variations. To this end, we conducted a comprehensive analysis of global tropical cyclone statistics for the satellite era (1970–2004). In each tropical ocean basin, we examined the numbers of tropical storms and hurricanes, the number of storm days, and the hurricane intensity distribution. The tropical cyclone data are derived from the best track archives

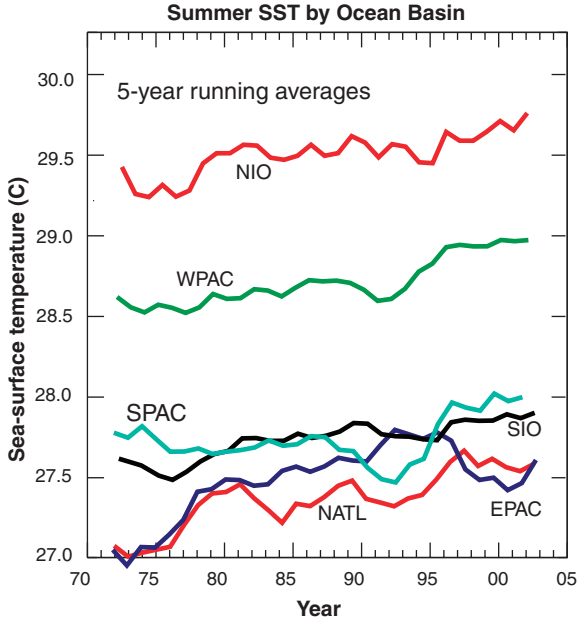

Fig. 1. Running 5-year mean of SST during the respective hurricane seasons for the principal ocean basins in which hurricanes occur: the North Atlantic Ocean (NATL: 90° to 20°E, 5° to 25°N, June-October), the Western Pacific Ocean (WPAC: 120° to 180°E, 5° to 20°N, May-December), the East Pacific Ocean (EPAC: 90° to 120°W, 5° to 20°N, June-October), the Southwest Pacific Ocean (SPAC: 155° to 180°E, 5° to 20°S, December-April), the North Indian Ocean (NIO: 55° to 90°E, 5° to 20°N, April-May and September-November), and the South Indian Ocean (SIO: 50° to 115°E, 5° to 20°S, November-April).

[1]School of Earth and Atmospheric Sciences, Georgia Institute of Technology, Atlanta, GA 30332, USA. [2]National Center for Atmospheric Research, Boulder, CO, USA.